JMEPEG (1998) 7:375-384

Microstructure of Heavily Deformed Magnesium-Lithium Composites Containing Steel Fibers

J.A. Jensen, F.C. Laabs, and L.S. Chumbley

(Submitted 13 November 1997; in revised form 26 January 1998)

The microstructure of deformation-processed metal-metal composites (DMMC) of Mg-Li alloys containing steel reinforcing fibers was characterized to correlate the fiber size to the deformation strain and mechanical properties of the composite material. Micrographs taken using scanning and transmission electron microscopy techniques revealed fiber sizes larger than predicted from the deformation applied to the bulk composite. Deformation strain in the fibers, therefore, was less than in the bulk material. Measurements from SEM and TEM micrographs were used to calculate the actual deformation strain present in the fibers. This strain was then used to adjust rule-of-mixture (ROM) predictions of the strength of the composite material. However, the experimental strengths of these materials were still less than the adjusted ROM values, potentially due to the presence of fibers considerably larger than the average size measured stereologically. Of the many models used to describe the strengthening observed in DMMC materials, the Hall-Petch relationship best describes the experimental data. Details of the strengthening models are discussed in relation to these composite materials.

Keywords in-situ composites, metal matrix composites, microscopy, steel wool

1. Introduction

Deformation processing of a mixture of two ductile phases to high levels of strain can result in wire or sheet composites with excellent mechanical properties. These composite materials are called in-situ composites or deformation-processed metal-metal composites (DMMC). Exceptionally high strengths were reported in face-centered cubic (fcc) copper alloys containing a body-centered cubic (bcc) metal as the reinforcing phase (e.g., Cu-20vol%Nb) that greatly exceeds rule-of-mixture (ROM) predictions for the strength of the composite (Ref 1-5). These results have prompted investigations of various DMMC materials based on titanium (Ref 6-9), magnesium (Ref 10, 11), and aluminum (Ref 12) alloy systems.

The high strengths observed in the copper-base DMMC at high levels of deformation have been attributed to the development of aligned, nanoscale bcc filaments embedded in the face-centered cubic (fcc) copper matrix (Ref 1-5). While some success has been achieved in aluminum-base DMMC systems (Ref 12), heavily deforming a composite of magnesium or magnesium-lithium containing steel fibers has produced sheet or rod with only moderate strengths (Ref 13). Similar results were observed in titanium-yttrium, and the moderate strengthening seen in these systems has been attributed to unique textures, which developed during deformation and affect the deformation characteristics and properties of the composite materials (Ref 6-11). In addition, nanoscale uniformity of the reinforcing filaments is a prerequisite for exceptionally high strengths in DMMC materials (Ref 1-5). Microstructural studies of the titanium-yttrium alloys revealed that the annealing procedure required to allow high levels of deformation resulted in rapid coarsening of the filamentary structure and a corresponding decrease in tensile strength.

The results of scanning electron microscopy (SEM) and transmission electron microscopy (TEM) studies that characterize and quantify the filament structure in the magnesium-base composites are presented here. The microstructures of composites prepared by infiltrating steel wool (iron) fibers with a molten magnesium-base matrix alloy (Ref 13) were examined. Earlier studies showed that these composites had unexpectedly low strengths, and it was hypothesized that the relatively coarse size of the steel (iron) fibers used in the preparation of the magnesium-base composite materials was adversely affecting the final filament size which can be achieved through deformation processing. The microstructural development as a function of amount and type of deformation is examined, and the scale of the filamentary structure is related to the strength of the composite.

2. Experimental Procedure

Composites of Mg-4Li/27Fe and Mg-12Li-2Nd/21Fe were prepared using a liquid metal infiltration casting method (Ref 13), where the following nomenclature was used: Mg-4Li/27Fe refers to a Mg-4wt%Li matrix containing 27 vol% fibers, and Mg-12Li-2Nd/21Fe refers to Mg-12wt%Li-2wt%Nd containing 21 vol% Fe. The fibers used in the composites were AISI 1011 steel wool. However, because the fibers are predominantly bcc due to the low carbon content, they are referred to as iron. Mg-4Li has a hexagonal close-packed (hcp) crystal structure, while Mg-12Li has a bcc structure. The composite materials were deformed by rolling, extrusion, and swaging at temperatures ranging from 20 to 400 °C.

Samples for SEM and TEM were obtained from sheet and rod samples at various levels of deformation. Scanning electron microscopy samples were prepared by standard metallographic

J.A. Jensen, F.C. Laabs, and **L.S. Chumbley,** Ames Laboratory (DOE) and the Department of Materials Science and Engineering, Iowa State University, Ames, IA 50011. Contact e-mail: jensen_jeff_a@cat.com.

methods and etched in a 2% nitric acid solution. The samples reacted quickly in water, requiring the use of alcohol- or oil-based polishing compounds for the final polishing steps. Ion milling the samples was sometimes necessary to remove oxide layers before placing the sample in the scanning electron microscope. Transmission electron microscopy foils were prepared by cutting slices of the rod or stacked sheets transverse to the direction of deformation. The TEM samples were polished with a dimpler and ion milled to remove oxide contamination before placing the sample in the transmission electron microscope. Table 1 shows the composite samples prepared for SEM and TEM examination. Samples were examined using Cambridge Stereoscan 200 (LEO Electron Microscopy Ltd., Cambridge, England), Amray 1845 FESEM (Amray, Bedford, MA), and JEOL 6100 SEM (JEOL Ltd., Tokyo, Japan) equipment and a Philips CM30 TEM microscope (FEI Co., Hillsboro, OR).

Quantitative stereological methods described by Underwood (Ref 14) were used to characterize the size and spacing of the iron filaments at various levels of deformation. The mean free distance (λ) between particles is given by:

$$\lambda = (1 - V_f)N \quad \text{(Eq 1)}$$

where V_f is the volume fraction of iron fibers and N is the number of interceptions with the iron fibers per unit length of test lines. V_f and N can both be determined by stereological methods, while V_f can also be determined from chemical analysis and density measurements. The previous equation is valid regardless of size, shape, or distribution of particles and is essentially the mean edge-to-edge distance between phases (Ref 14). Equation 1 provides a relatively easy measurement technique for describing the interparticle distance in a two-phase material. Because the number of interceptions with the fibers is the same as the number of interceptions with the matrix, the average thickness of the fibers, t, can be estimated by:

$$t = (1 - V_m)/N \quad \text{(Eq 2)}$$

where V_m is the volume fraction of the matrix. These equations allow simple determination of the size and spacing of filaments in a composite material at various levels of deformation.

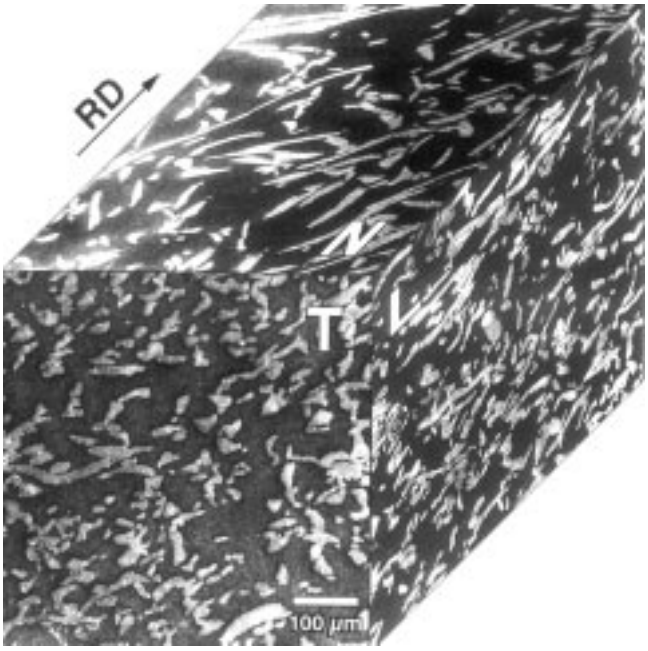

Fig. 1 Scanning electron microscopy micrographs of hcp/bcc Mg-4Li/27Fe as cast. The rolling direction (RD) and the sheet normal (N), transverse (T), and longitudinal (L) sections are indicated.

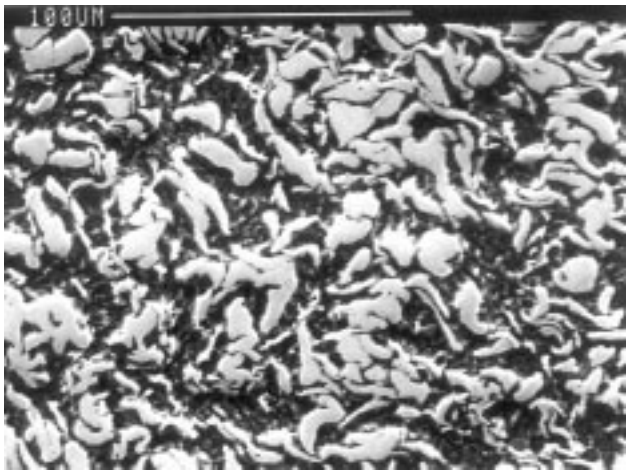

Fig. 2 Scanning electron microscopy micrograph of the hcp/bcc Mg-4Li/27Fe rod extruded at 350 °C to $\eta = 2.7$ (transverse section)

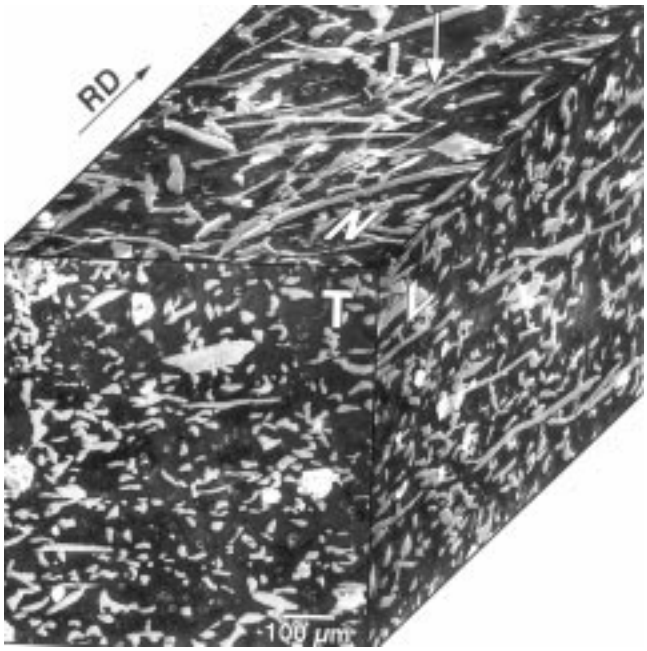

Fig. 3 Scanning electron microscopy micrographs of bcc/bcc Mg-12Li-2Nd/21Fe as cast. The rolling direction (RD) and the sheet normal (N), transverse (T), and longitudinal (L) sections are indicated.

In this paper, the true deformation strain of the wire is given by:

$$\eta = 2 \ln (d_0/d_f) \quad \text{(Eq 3)}$$

where d_0 and d_f are the initial and final diameters, respectively. For sheet material, the true deformation strain is given by:

$$\eta = \ln (t_0/t_f) \quad \text{(Eq 4)}$$

where t_0 and t_f are the initial and final thickness, respectively. Because the production of sheet and rod requires different deformation modes with different stress-strain relations, an effective deformation strain is calculated for sheet material so that comparison can be made to rod materials at a true strain of η. For rolled sheet with inhibited spread, an effective deformation strain is calculated as $\eta_e = (2/\sqrt{3})\eta$ and is comparable to the true deformation strain for rod materials (Ref 15). Deformation can also be presented as a percent reduction in thickness (%RT) for sheet materials or as a percent reduction in cross-sectional area (%RA) for rod materials.

3. Results

3.1 hcp/bcc Microstructure

Figure 1 shows the Mg-4Li/27Fe composite prepared by infiltration casting. Minimal porosity and good fiber wetting were characteristic of this casting process. The sheet material exhibited poor formability, failing catastrophically after a 50 to 75% rolling reduction at 400 °C. Due to the poor rolling characteristics of the Mg-4Li/27Fe sheet, this material was not studied. The Mg-4Li/27Fe rod was deformed at 350 to 375 °C to $\eta = 3.92$ and characterized.

Figure 2 shows the Mg-4Li/27Fe composite extruded at 350 °C to a deformation strain of $\eta = 2.7$. Scanning electron microscopy shows that the iron fibers are thinning and elongating as a result of the deformation. The fibers are also convoluting around the axis of deformation, which may indicate that the

Table 1 Samples for SEM and TEM characterization

Composite	Deformation type	Deformation strain(a), η	Reduction, %	Observation method
Mg-12Li-2Nd/21Fe	As cast	…	…	SEM
	Sheet	1.89	80.5, RT	SEM, TEM
	Sheet	3.67	95.8, RT	TEM
	Sheet	3.97	96.8, RT	SEM
	Sheet	5.55	99.2, RT	TEM
	Sheet	6.54	99.7, RT	SEM, TEM
	Sheet	8.60	99.94, RT	…
	Rod	3.07	95.4, RA	SEM, TEM
	Rod	4.29	98.6, RA	SEM, TEM
	Rod	5.98	99.7, RA	SEM, TEM
Mg-4Li/27Fe	As cast	…	…	SEM
	Rod	2.69	93.2, RA	SEM
	Rod	3.92	98.0, RA	SEM

(a) η_e, sheet. (b) RT, reduction in thickness, RA, reduction in area

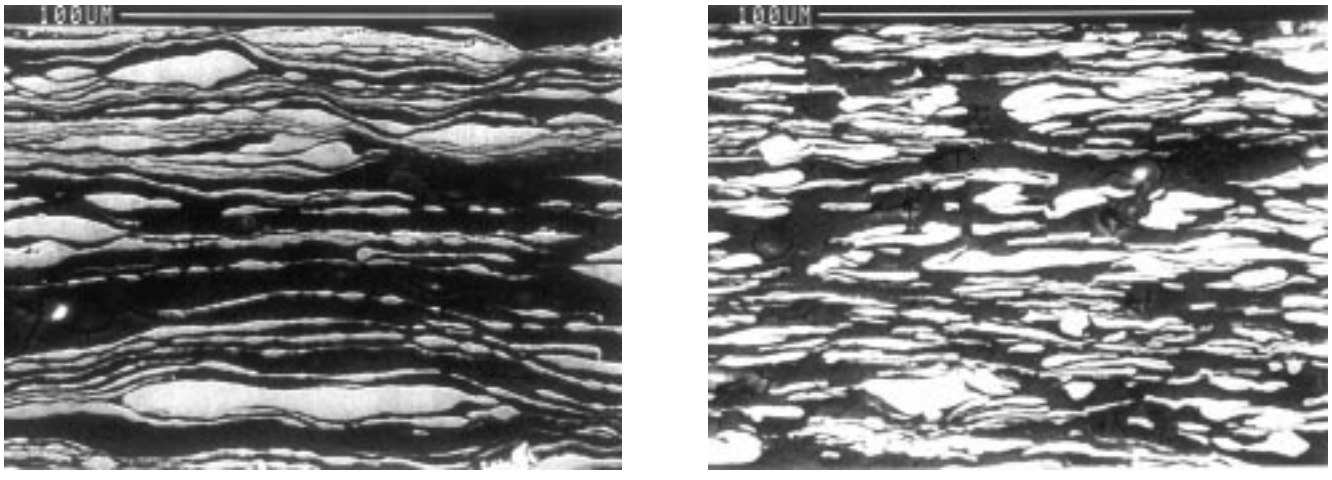

(a) **(b)**

Fig. 4 Scanning electron microscopy micrographs showing the longitudinal (a) and transverse (b) sections of the bcc/bcc Mg-12Li-2Nd/21Fe sheet rolled to $\eta_e = 4.0$ at room temperature

iron is beginning to develop a <110> fiber texture. These trends continued as the rod material was swaged at 375 to 400 °C to a deformation strain of $\eta = 3.92$. Additional hot swaging resulted in a rod with numerous internal cracks that could not reliably be mechanically tested.

3.2 bcc/bcc Microstructure

Figure 3 shows the Mg-12Li-2Nd/21Fe as-cast composite structure. Note the nonuniform size of the iron fibers in the initial casting. A small amount of an intermetallic phase, assumed to be Fe_2Nd formed by the 640 °C eutectic reaction during solidification (Ref 16), was also present and is shown between some of the larger iron fibers (arrowed). Figures 4 and 5 illustrate the microstructure at various stages of rolling at room temperature. Figure 4 shows SEM micrographs of the sheet material rolled to $\eta_e = 4.0$. The iron fiber structure is evident and continues to be refined as rolling proceeds (Fig. 5). Note that while a range of fiber sizes is shown in Fig. 5, the resolution limit of the SEM makes any quantitative measurements of the smallest fibers suspect. At these higher values of magnification, it becomes necessary to use TEM to obtain accurate measurements of filament sizes.

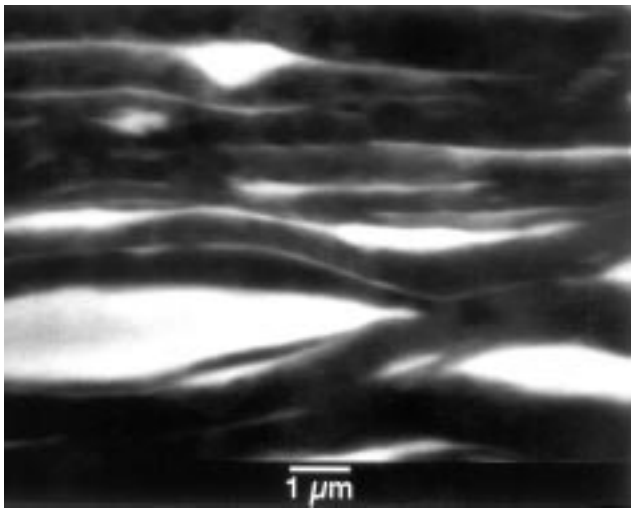

Fig. 5 Scanning electron microscopy micrograph of a transverse section of the bcc/bcc Mg-12Li-2Nd/21Fe sheet rolled to $\eta_e = 6.5$ at room temperature

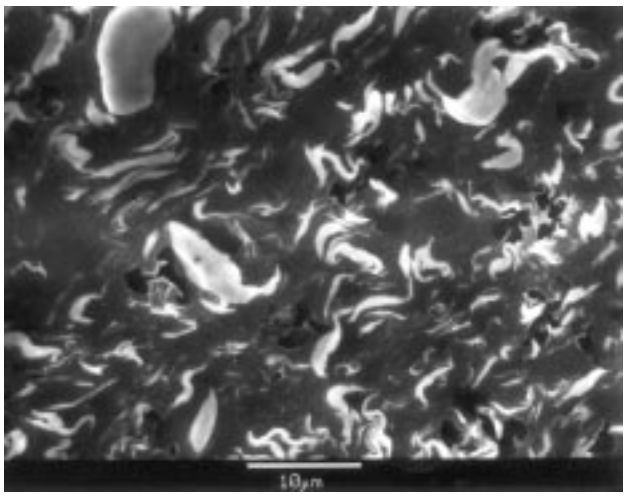

Fig. 7 Scanning electron microscopy micrograph of bcc/bcc Mg-12Li-2Nd/21Fe rod swaged to $\eta = 6.0$ at room temperature (transverse section)

Fig. 6 Montage of bright-field transmission electron microscopy micrographs of bcc/bcc Mg-12Li-2Nd/21Fe sheet rolled to $\eta_e = 6.5$ at room temperature (transverse section)

When TEM micrographs are characterized with quantitative stereology, it is often helpful to create a montage of overlapping micrographs. The montage presents a larger area of the sample and facilitates more valid quantitative measurements of the bulk material. A montage of TEM micrographs (Fig. 6), for the Mg-12Li-2Nd/21Fe sheet rolled to $\eta_e = 6.5$ at room temperature, shows the considerable difference in size observed for the smallest and largest iron filaments in the highly deformed sheet material. While some of the filaments are <100 nm thick, others are still 5 to 10 μm thick.

The Mg-12Li-2Nd/21Fe composite was also swaged at room temperature. While cracks started to appear in sections of the rod after $\eta = 3.1$, one piece free of cracks was swaged to $\eta = 6.0$. Figure 7 shows an SEM micrograph of this sample. Note that the elongated iron fibers are curling around the axis of deformation, which indicates that the iron is developing a <110> fiber axis. Figure 8 shows a montage of dark-field TEM micrographs of the Mg-12Li-2Nd/21Fe rod swaged at room temperature to $\eta = 6.0$.

3.3 Microstructural Analysis

Bulk density measurements showed that the volume fraction of iron fibers in the composite material was 27 and 21 vol% for the Mg-4Li/27Fe and Mg-12Li-2Nd/21Fe castings, respectively. These values were used to determine the phase sizes quoted. Although these measurements represent an average of the entire sample, rather than being specific for each micrograph evaluated, the general trends observed in fiber size remain unchanged. The use of a fixed value for volume fraction, rather than using quantitative microscopy techniques to determine a specific value for each micrograph taken, gave more flexibility during the reevaluation of tensile data predictions for the composite materials.

To determine the number of intercepts per length, N, two concentric circles of known circumferential lengths were printed on a transparency and placed over each micrograph. The number of intersections of these circles with iron fibers was counted, and the sum was divided by the total length of the circles. Multiple intersections of the circles with the same iron fibers were counted as separate intersections, as specified by Ref 14. This number for N was then used to determine the size and spacing of the iron fibers, t and λ, respectively. A value for N was determined for each micrograph and used to determine all reported phase sizes.

In general, the phase sizes and volume fractions measured from SEM and TEM micrographs agreed at all levels of deformation. Therefore, the data contained in the graphs are not specified as being derived from SEM or TEM measurements. Data plotted on the graphs indicate the average values, while the error bars present for some of the data indicate a ±1 standard deviation from the average value.

3.4 hcp/bcc Composite Analysis

Based on the definitions of true strain, Eq 3 can be rearranged to predict the fiber size in a rod material for a given level of deformation:

$$d = d_0 \exp(-\eta/2) \quad \text{(Eq 5)}$$

where d_0 is the initial fiber size and d is the fiber size at a given deformation level (η). Similarly, Eq 4 can be rearranged to predict the fiber size in a sheet material:

$$t = t_0 \exp(-\sqrt{3}\eta_e/2) \quad \text{(Eq 6)}$$

where t_0 is the initial fiber size and t is the fiber size at a given deformation level (η_e). These equations assume that the matrix and fiber phases deform in proportion to the amount of deformation applied to the bulk composite material. These predictions can be used as a baseline for evaluating the quantitative stereology measurements of phase size.

Figure 9 shows the decrease in iron fiber size for the deformed Mg-4Li/27Fe rod material. The lines labeled "t pred" indicate the minimum and maximum predicted iron fiber size assuming that the matrix and fibers perfectly codeformed. The minimum predicted fiber size is directly related to the external shape change of the composite material (Eq 5 and 6). For example, a 200 fold reduction in sheet thickness would be expected

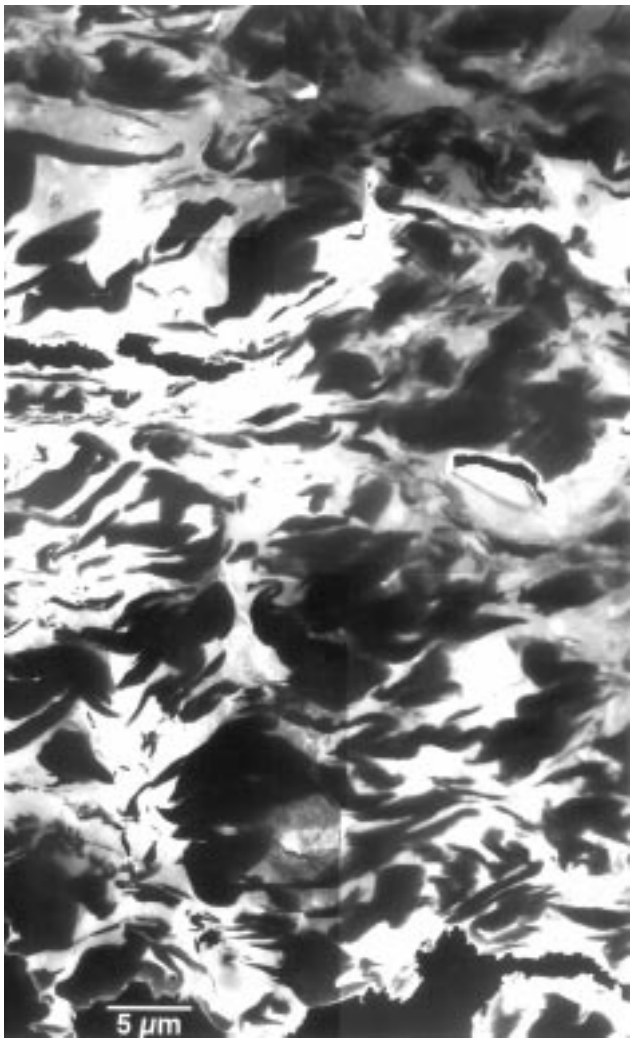

Fig. 8 Montage of dark-field transmission electron microscopy micrographs of bcc/bcc Mg-12Li-2Nd/21Fe rod swaged to $\eta = 6.0$ at room temperature (transverse section)

to reduce the fiber thickness by a factor of 200. The maximum predicted fiber size takes into account that stereological techniques to determine fiber size yield an equivalent fiber diameter rather than a true fiber thickness. For very thin ribbon-shaped filaments, as in the case of heavily deformed rod and sheet, mathematical analysis of the stereological techniques reveals that this diameter is equal to double the filament thickness (Ref 14). The minimum and maximum lines are intended to give a range of predicted filament sizes, which should provide an envelope for the stereologically measured values. The average fiber sizes measured for Mg-4Li/27Fe rod (Fig. 9) fall within the predicted range of values.

3.5 bcc/bcc Composite Analysis

Figures 10 and 11 show the measured and predicted iron fiber sizes for Mg-12Li-2Nd/21Fe rod and sheet, respectively. The measured fiber sizes for the Mg-12Li-2Nd/21Fe rod material are within experimental error of the predicted range of sizes (Fig. 10). However, the average fiber sizes measured in the Mg-12Li-2Nd/21Fe sheet material (Fig. 11) deviate by nearly an order of magnitude from the predicted range of values at high-deformation levels. Because the fibers are not deforming at the same rate as the bulk composite during rolling, it is evident that axisymmetric deformation is more efficient than rolling at reducing the size of the filaments in these magnesium-base composite materials.

In the bcc/bcc Mg-12Li-2Nd/21Fe sheet, stereological measurements indicate that the sizes of both the matrix and fibers are larger than predicted, which implies that both phases have deformed less than the bulk composite material. For a given reduction in area for a composite material, it seems intuitive that if one phase is larger than predicted, then the other phase should be smaller than the predicted size. This apparent discrepancy between the stereological measurements and the predicted phase sizes has also been noted in other systems, such as copper-niobium and pearlite (Ref 5, 17). While various reasons were given in these studies, discrepancies are believed to be related to the difference between the stereological definition of fiber size, which determines an equivalent three-dimensional fiber diameter, and the predicted thickness of the ribbon-shaped filaments in the composite material, which is based on a one-dimensional reduction in fiber thickness.

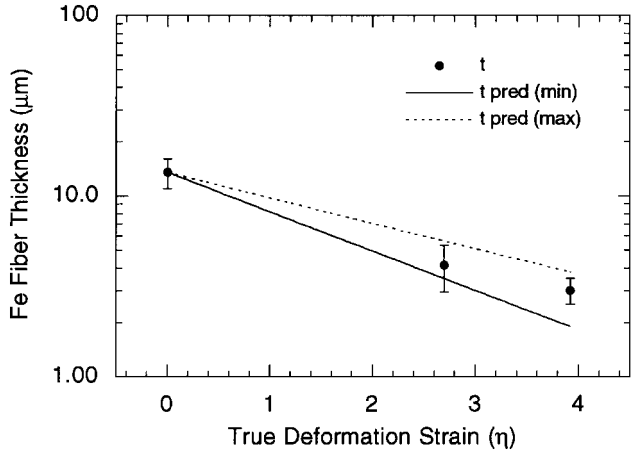

Fig. 9 Measured iron fiber size (*t*) and the minimum and maximum predicted fiber sizes (*t* pred) for hcp/bcc Mg-4Li/27Fe rod

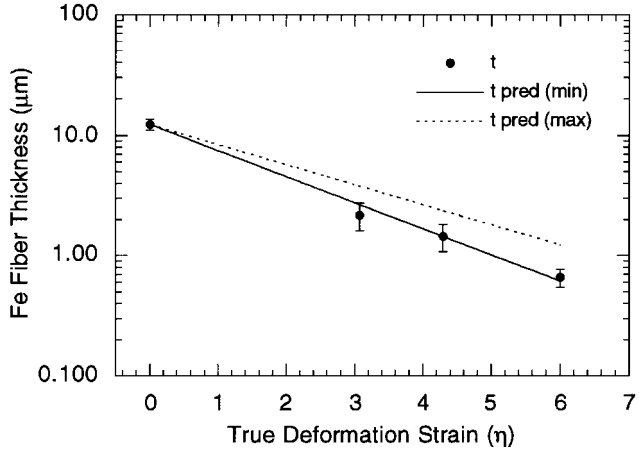

Fig. 10 Measured iron fiber size (*t*) and the predicted fiber size (*t* pred) for bcc/bcc Mg-12Li-2Nd/21Fe rod. Note: tensile data at $\eta = 6$ is invalid due to internal cracking.

4. Discussion

4.1 Tensile Strength and ROM Strength Predictions

Tensile properties of Mg-4Li/27Fe rod and Mg-12Li-2Nd/21Fe sheet and rod have been previously reported (Ref 13). In that study the predicted ROM tensile strengths for the Mg-4Li/27Fe rod and Mg-12Li-2Nd/21Fe rod and sheet exceeded the experimental strength of the composite materials. For Mg-12Li-2Nd/21Fe sheet, the reason for the discrepancy between the actual and predicted strengths of the composite reported in Ref 13 can be partially explained. The ROM predictions were based on the assumption that the matrix and fibers deform in direct proportion to the amount of deformation applied to the bulk composite. In the case of the Mg-12Li-2Nd/21Fe sheet,

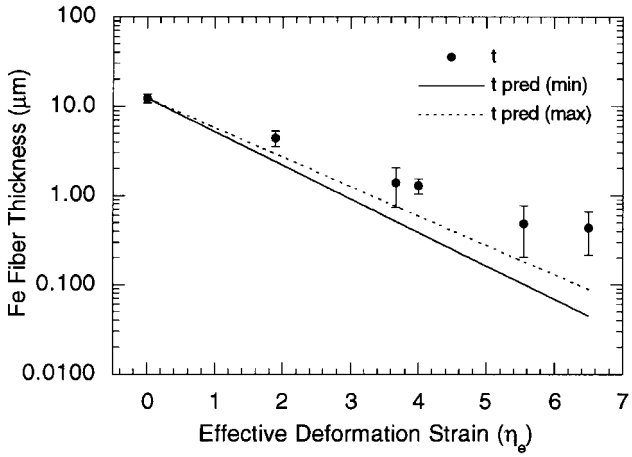

Fig. 11 Measured iron fiber size (*t*) and the predicted fiber size (*t* pred) for bcc/bcc Mg-12Li-2Nd/21Fe sheet

the iron fibers are larger than predicted from bulk deformation levels (Table 2), so the actual amount of deformation experienced by the fibers should be considered. For example, the average measured fiber size in the Mg-12Li-2Nd/21Fe casting was 12.4 μm. If the fiber thickness was reduced in proportion to the composite sheet thickness reduction, the iron fiber size would be 0.39 μm in the $\eta_e = 4.0$ sheet material. However, the average size measured stereologically in the sheet material at $\eta_e = 4.0$ was 1.30 μm. This fiber size actually corresponds to a deformation strain of $\eta_e = 2.6$. Table 2 summarizes modified η_e values for the iron phase in Mg-12Li-2Nd/21Fe sheet.

The data in Table 2 can also be depicted graphically (Fig. 12). This figure shows that the amount of actual deformation in the iron fibers was less than the amount of deformation experienced by the composite during rolling. The values labeled predicted directly correspond to the external shape change of the composite, while the values labeled actual indicate the amount of deformation in the fibers based on the observed fiber size. The error bars represent the values calculated using the average fiber size ±1 standard deviation.

In contrast to the rod material, where the size of the iron fibers in the Mg-4Li/27Fe and Mg-12Li-2Nd/21Fe rods closely match the predicted values, the Mg-12Li-2Nd/21Fe sheet data (Fig. 12) show that the deformation of the iron fibers is less than the deformation of the bulk composite sheet material, so a smaller η_e value can be ascribed to the iron phase. The original ROM predictions for the Mg-12Li-2Nd/21Fe sheet material can then be adjusted to reflect the actual amount of deformation in the iron fibers. For example, the strength of the AISI 1011 steel sheet at $\eta_e = 4.0$ was approximately 1077 MPa, while the strength at $\eta_e = 2.6$ was only 920 MPa. Adjusting for the volume fraction of fibers in the composite, the actual strain in the fibers would reduce the previous ROM prediction by 33 MPa, from 338 to 305 MPa.

Figure 13 shows the original and adjusted ROM strength predictions for the Mg-12Li-2Nd/21Fe sheet material. The deformation strain in this figure represents the deformation of the bulk Mg-12Li-2Nd/21Fe composite sheet, while the adjusted ROM values correct for the actual strain in the iron fibers. The error bars for the adjusted ROM values represent calculations based on the average fiber size ±1 standard deviation. No error bars are shown at $\eta_e = 8.6$ because this material was not characterized with SEM or TEM. The adjusted ROM tensile strength for the $\eta_e = 8.6$ material was extrapolated from the best-fit ROM line for $\eta_e \leq 6.5$.

In the case of the Mg-12Li-2Nd/21Fe sheet, adjusting the ROM calculations to account for actual deformation of the iron fibers results in predicted values that more closely match the experimental tensile strength, especially at higher deformation levels. However, the ROM predictions are still higher than the actual strength of the Mg-12Li-2Nd/21Fe composite sheet, as are the ROM values for the rod material, which needed no adjustment.

Table 2 Predicted and actual iron fiber size and deformation strain

Material	Predicted fiber deformation strain, η_e	Minimum predicted fiber size(a), μm	Actual fiber size(b), μm	Actual fiber deformation strain, η_e
Mg-12Li-2Nd/21Fe sheet	0.00	12.37	12.37 ± 1.34	0.00
	1.89	2.41	4.43 ± 0.87	1.19
	3.67	0.52	1.39 ± 0.66	2.52
	4.00	0.39	1.30 ± 0.24	2.60
	5.55	0.10	0.49 ± 0.29	3.73
	6.50	0.04	0.44 ± 0.22	3.86

(a) Based on reduction in composite sheet thickness. (b) ± one standard deviation

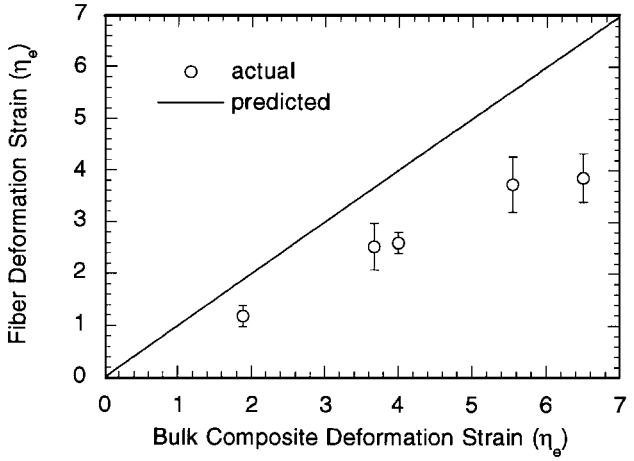

Fig. 12 Predicted deformation strain of the iron filaments in rolled bcc/bcc Mg-12Li-2Nd/21Fe sheet and actual strain based on fiber size measurements

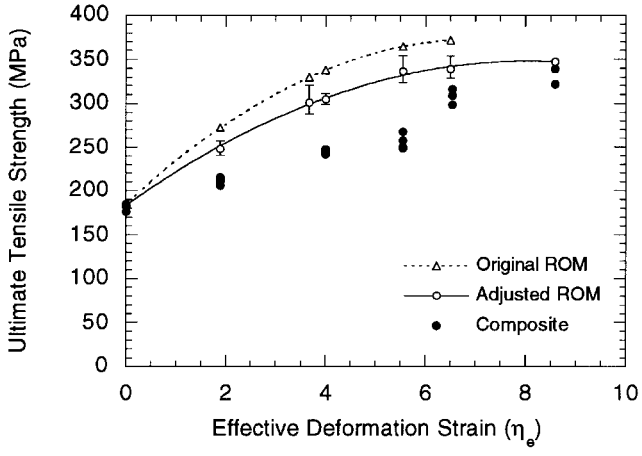

Fig. 13 Rule of mixture strength predictions for Mg-12Li-2Nd/21Fe sheet adjusted for the actual deformation of the iron fibers

The adjusted ROM predictions shown in Fig. 13 only account for the actual deformation of the iron fibers. The actual deformation of the matrix was not considered because the strength of the iron fibers is the dominant factor in the ROM calculations. For example, adjusting for volume fractions, the effect of the iron strength on the ROM predictions is three to four times greater than the strength of the Mg-12Li-2Nd matrix. Adjusting for the actual amount of deformation in the matrix phase would slightly decrease the ROM predictions.

4.2 Strengthening Relationships

Materials often exhibit a Hall-Petch type of strengthening relationship of the form:

$$\sigma = \sigma_0 + kd^{-n} \quad \text{(Eq 8)}$$

where σ is ultimate tensile stress, σ_0 is friction stress, d is average grain size (or filament or spacing), k is a fitting parameter, and $n = -\frac{1}{2}$ ideally (Ref 18-20). This relationship is usually demonstrated by plotting the yield strength of a material versus the inverse square root of the grain size. This equation can also be used to describe the grain size dependence of several other materials parameters, for example, tensile strength, fracture stress, and fatigue strength. The theory is based on the concept that grain boundaries act as barriers to dislocation motion (Ref 20). In DMMC materials, the size and spacing of the reinforcing filaments can be substituted for the grain size in Eq 8 because the matrix-fiber interface acts to block the motion of dislocations.

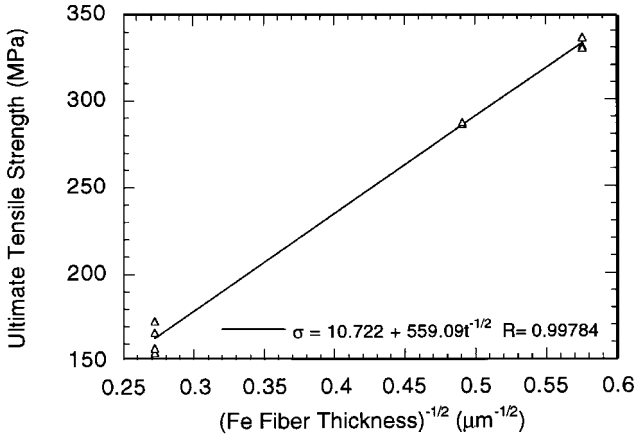

Fig. 14 Hall-Petch fit for Mg-4Li/27Fe rod tensile strength

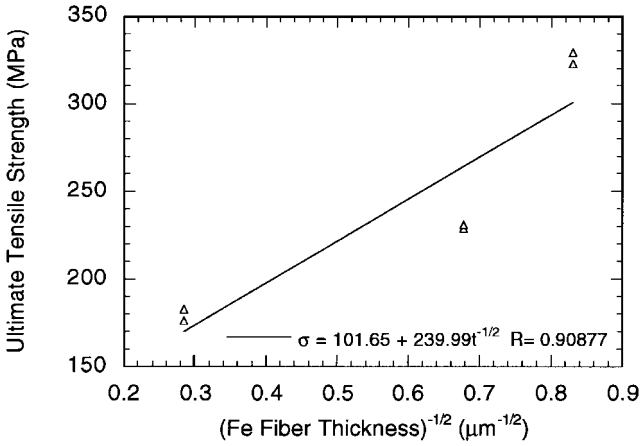

Fig. 15 Hall-Petch fit for Mg-12Li-2Nd/21Fe rod tensile strength

Figure 14 shows that the tensile data for the hcp/bcc Mg-4Li/27Fe rod material fits the Hall-Petch relationship (correlation coefficient, $R = 0.998$). However, the value for σ_0 is only 11 MPa. A more reasonable value expected for σ_0 is the as-cast tensile strength of the composite material, which in the case of Mg-4Li/27Fe was ~163 MPa, or the predicted ROM strength of the Mg-4Li/27Fe casting, which was 200 MPa. To be more conservative, σ_0 could be approximated as 125 MPa, the as-cast strength of the matrix, because the formation and propagation of dislocations would most likely be concentrated in the softer matrix phase. In any case, the value for σ_0 obtained empirically from the Hall-Petch equation falls far below any of these values.

Figures 15 and 16, respectively, show the Hall-Petch relationships for the bcc/bcc Mg-12Li-2Nd/21Fe rod and sheet materials. Note that the correlation is lower ($R = 0.909$) for the Mg-12Li-2Nd/21Fe rod than it was for the Mg-4Li-27Fe rod, but the empirically determined value for σ_0, 101 MPa, is approximately equal to the strength of the Mg-12Li-2Nd matrix (106 MPa). The Mg-12Li-2Nd/21Fe sheet material closely follows the Hall-Petch relationship ($R = 0.990$), and the value determined for σ_0 is 159 MPa, which is reasonably close to the as-cast tensile strength of the composite (180 MPa).

Other strengthening models have been developed to describe the mechanical behavior of highly deformed composite materials. For example, Embury and Fisher (Ref 21) developed a modified Hall-Petch relationship to describe the strength of pearlitic steel wire. The Embury-Fisher model requires measurement of only the initial fiber size (or spacing) and then relies on the assumption that the fiber size (or spacing) is reduced at the same fractional amount as the bulk material to predict the strength of that material. However, the fiber sizes in the Mg-12Li-2Nd/21Fe sheet are considerably larger than predicted from the deformation of

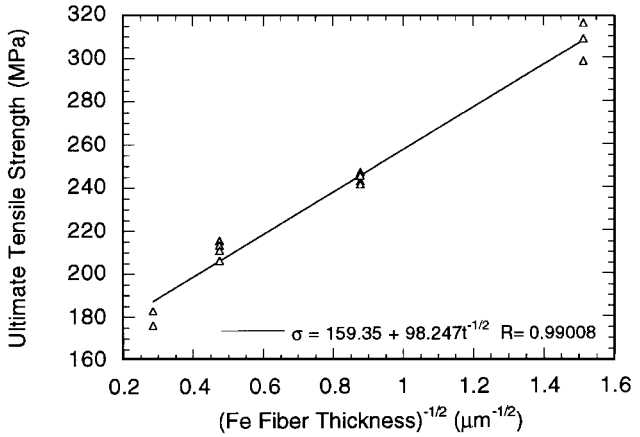

Fig. 16 Hall-Petch fit for Mg-12Li-2Nd/21Fe sheet tensile strength

the bulk material, and using the Embury-Fisher model results in a worse fit to the experimental data.

Fitting the data for Mg-4Li/27Fe and Mg-12Li-2Nd/21Fe rod materials using the Embury-Fisher model produces results similar to Hall-Petch, which is expected because the fiber size in these materials is close to the sizes predicted from the bulk deformation. Modeling the Mg-4Li/27Fe rod data with the Embury-Fisher equation yields a value for σ_0 of 63 MPa, significantly higher than the value of 11 MPa determined using Hall-Petch. The Hall-Petch fit for Mg-4Li/27Fe rod used the fiber size data points shown in Fig. 9, while the Embury-Fisher fit used the minimum predicted fiber size in the same figure (the line marked *t* pred (min)). Subtle variations in the fiber size can make a considerable impact on the final results, so caution should be taken when using the Embury-Fisher model to ensure that the experimental size and spacing of the barrier phase actually correspond to the deformation of the bulk material.

Gil Sevillano (Ref 22) also developed a strengthening model for pearlitic steels that was later adapted for heavily deformed Cu-20Nb wire (Ref 2). The model presented in Ref 2 was a ROM relationship (Eq 7) that included additional strengthening terms. The modified ROM model in Ref 2 and other strengthening models used to describe the exceptionally high strengths observed in some DMMC materials (Ref 23) are not applicable to the Mg-4Li/27Fe and Mg-12Li-2Nd/21Fe materials, because experimental tensile data were less than the ROM predictions.

In general, the Hall-Petch model adequately describes the strengthening observed in the heavily deformed Mg-12Li-2Nd/21Fe sheet material. Hall-Petch also fits the data for Mg-4Li/27Fe and Mg-12Li-2Nd/21Fe rod materials, but with less certainty. Poor formability of the Mg-4Li/27Fe and Mg-12Li-2Nd/21Fe rod materials hindered more thorough analysis. Additional data are needed to validate the strengthening models for these materials.

4.3 Microstructure

The data shown in Fig. 9 to 11 presented the average fiber size determined stereologically, with error bars corresponding to ±1 standard deviation. However, as is true of many real distributions, data exist which fall outside the error bars. The size of the largest observed iron fiber from each micrograph was recorded and averaged for each composite material at each level of deformation. Figures 17 to 19 include the average maximum fiber size observed (*t* max average) as well as the maximum fiber observed (*t* max observed). The largest iron fibers in the Mg-4Li/27Fe and Mg-12Li-2Nd/21Fe composite materials are substantially larger than both the predicted sizes and the average fiber sizes measured. For example, in the Mg-12Li-2Nd/21Fe sheet material at $\eta_e = 6.5$, where the maximum predicted thickness was 0.088 μm, the largest observed iron fiber from among all of the micrographs was 12.7 μm. Considering that the Mg-12Li-2Nd/21Fe sheet was 165 μm (0.0065 in.) thick, a 12.7 μm iron fiber presents a potentially large stress concentrator during mechanical testing, because the fiber size is 7.7% of the sheet thickness.

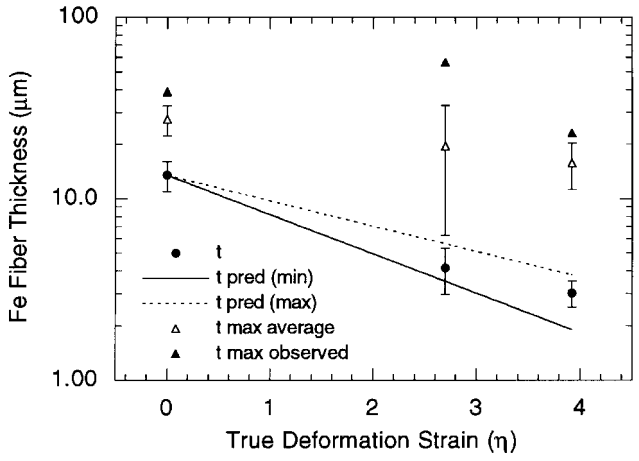

Fig. 17 Variation of iron fiber sizes in hcp/bcc Mg-4Li/27Fe rod

5. Conclusions

- In the bcc/bcc Mg-12Li-2Nd/21Fe sheet material, the measured fiber sizes were larger than predicted for the deformation applied to the bulk composite, indicating that the

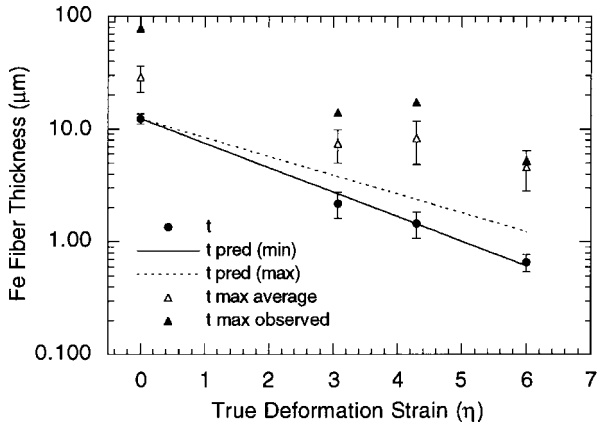

Fig. 18 Variation of iron fiber sizes in bcc/bcc Mg-12Li-2Nd/21Fe rod. Note: tensile data at $\eta = 6$ was invalid due to internal cracking.

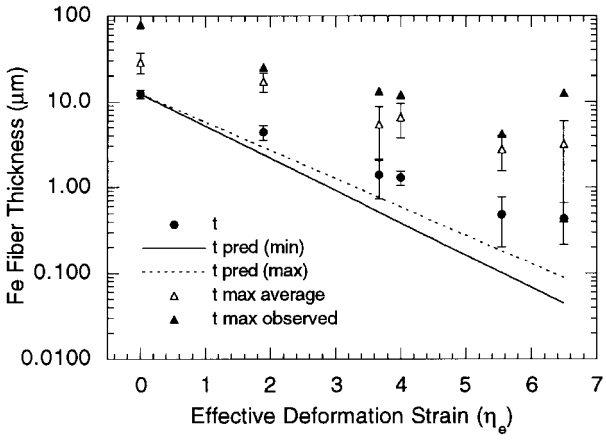

Fig. 19 Variation of iron fiber sizes in bcc/bcc Mg-12Li-2Nd/21Fe sheet

strain in the fibers was less than the bulk deformation. In the Mg-4Li/27Fe and Mg-12Li-2Nd/21Fe rod materials, the measured sizes were within the range of predicted values.

- The experimental strengths of these composite materials were less than the strengths predicted from ROM calculations. The ROM values for the Mg-12Li-2Nd/21Fe sheet were adjusted to account for the large fiber sizes and the actual deformation strain in the fibers; however, the adjusted ROM predictions were still lower than the experimental data.
- The Hall-Petch model adequately describes the strengthening observed in the Mg-12Li-2Nd/21Fe sheet. The Hall-Petch model also fit the data for the Mg-4Li-27Fe and Mg-12Li-2Nd/21Fe rod materials, although with less certainty. The physical data obtained for these composite materials negated the use of other strengthening models often used to describe the strengthening observed in other DMMC materials.
- The presence of extremely large fibers, apparently unaffected by any of the mechanical deformation processes, can act as stress concentration points causing the composites to fail at lower values than predicted by ROM calculations.

Acknowledgments

The authors thank H. Sailsbury and L. Keehner for valuable assistance. This work was performed for the U.S. Department of Energy at Ames Laboratory, Iowa State University, under contract No. W-7405-Eng-82. Research was supported by the Director of Energy Research (Office of Basic Energy Sciences), the Office of Naval Research Graduate Fellowship Program, and the Boeing Graduate Fellowship Program.

References

1. J. Bevk, J.P. Harbison, and J.L. Bell, Anomalous Increase in Strength of In Situ Formed Cu-Nb Multifilamentary Composites, *J. Appl. Phys.*, Vol 49 (No. 12), 1978, p 6031-6038
2. J.D. Verhoeven, L.S. Chumbley, F.C. Laabs, and W.A. Spitzig, Measurement of Filament Spacing in Deformation Processed Cu-Nb Alloys, *Acta Metall.*, Vol 39 (No. 11), 1991, p 2825-2834
3. J.D. Verhoeven, W.A. Spitzig, L.L. Jones, H.L. Downing, C.L. Trybus, E.D. Gibson, L.S. Chumbley, L.G. Fritzmeier, and G.D. Schnittgrund, Development of Deformation Processed Copper-Refractor Metal Composite Alloys, *J. Mater. Eng.*, Vol 12 (No. 2), 1990, p 127-139
4. W.A. Spitzig, A.R. Pelton, and F.C. Laabs, Characterization of the Strength and Microstructure of Heavily Cold Worked Cu-Nb Composites, *Acta Metall.*, Vol 35 (No. 10), 1987, p 2427-2442
5. C.L. Trybus, " Microstructure-Strength Relationships of Heavily Deformed Cu-Based Composites," Ph.D. dissertation, Iowa State University, 1988
6. A.M. Russell, Microstructure-Strength Relationships of a Deformation Processed Titanium-Yttrium Composite, Ph.D. dissertation, Iowa State University, 1994
7. A.M. Russell, T.W. Ellis, and L.S. Chumbley, In-Situ Strengthening of Titanium with Yttrium, *J. Mater. Sci.*, Vol 30, 1995, p 2070-2076
8. A.M. Russell, L.S. Chumbley, T.W. Ellis, F.C. Laabs, B. Norris, and G.E. Donizetti, In-Situ Strengthening of Titanium with Yttrium: Texture Analysis, *J. Mater. Sci.*, Vol 30, 1995, p 4249-4262
9. A.M. Russell, J.A. Jensen, L.S. Chumbley, D.G. Konitzer, and T.W. Ellis, In-Situ Strengthening in Titanium, *Titanium '92: Science and Technology*, F. Froes and I. Caplan, Ed., TMS, 1993, p 407-414
10. J.A. Jensen, A.M. Russell, T.W. Ellis, and L.S. Chumbley, Magnesium-Based Metal-Metal Composites, *Aluminum and Magnesium for Automotive Applications*, J.D. Bryant and D.R. White, Ed., TMS, 1996, p 173-187
11. J.A. Jensen, A.M. Russell, T.W. Ellis, and L.S. Chumbley, HCP Matrix In-Situ Composites, *Light Metals 1995*, J. Evans, Ed., TMS, 1995, p 1367-1374
12. A.M. Russell and L.S. Chumbley, Aluminum-Based In-Situ Composites, unpublished research, Ames Laboratory and Iowa State University, 1996-1997
13. J.A. Jensen and L.S. Chumbley, Processing and Mechanical Properties of Magnesium-Lithium Composites Containing Steel Fibers, *Met. and Mat. Trans.*, Vol 29A, 1998, p 863-873
14. E.E. Underwood, *Quantitative Stereology*, Addison-Wesley, 1970, p 80-93
15. W. Johnson and P.B. Mellor, *Engineering Plasticity*, Van Nostrand Reinhold, New York, 1973, p 109-110
16. T.B. Massalski, *Binary Alloy Phase Diagrams*, ASM International, 1990, p 1085
17. G. Langford, Deformation of Pearlite, *Met. Trans. A*, Vol 8, 1977, p 861-875
18. E.O. Hall, The Deformation and Ageing of Mild Steel: III Discussion and Results, *Proc. Phys. Soc.*, Vol B (No. 64), 1951, p 747-753
19. N.J. Petch, The Ductile Fracture of Polycrystalline α-Iron, *Philos. Mag.*, Vol 1, 1956, p 186
20. G.E. Dieter, *Mechanical Metallurgy*, McGraw-Hill, 1986, p 189-191
21. J.D. Embury and R.M. Fisher, The Structure and Properties of Drawn Pearlite, *Acta Metall.*, Vol 14, 1966, p 147-159
22. J. Gil Sevillano, On the Yield and Flow Stress of Lamellar Pearlite, *Strength of Metals and Alloys, Proc. ICSMA 5*, P. Haasen, V. Gerold, and G. Kowtorz, Ed., Pergamon Press, 1980, p 819
23. J.D. Embury, Micromechanical Descriptions of Heavily Deformed Materials, *Scripta Metall.*, Vol 27, 1992, p 981-986